

Q-RepEx: A Python pipeline to increase the sampling of empirical valence bond simulations

Sebastian Brickel^{a,1}, Andrey O. Demkiv^a, Rory M. Crean^a, Gaspar P. Pinto^a,
Shina Caroline Lynn Kamerlin^{a,b,*}

^a Department of Chemistry – BMC, Uppsala University, BMC Box 576, S-751 23, Uppsala, Sweden

^b School of Chemistry and Biochemistry, Georgia Institute of Technology, 901 Atlantic Drive NW, Atlanta, GA, 30332-0400, USA

ARTICLE INFO

Keywords:

Enhanced sampling
Empirical valence bond
Free energy perturbation
Replica exchange molecular dynamics
Q6

ABSTRACT

The exploration of chemical systems occurs on complex energy landscapes. Comprehensively sampling rugged energy landscapes with many local minima is a common problem for molecular dynamics simulations. These multiple local minima trap the dynamic system, preventing efficient sampling. This is a particular challenge for large biochemical systems with many degrees of freedom. Replica exchange molecular dynamics (REMD) is an approach that accelerates the exploration of the conformational space of a system, and thus can be used to enhance the sampling of complex biomolecular processes. In parallel, the empirical valence bond (EVB) approach is a powerful approach for modeling chemical reactivity in biomolecular systems. Here, we present an open-source Python-based tool that interfaces with the *Q* simulation package, and increases the sampling efficiency of the EVB free energy perturbation/umbrella sampling approach by means of REMD. This approach, *Q-RepEx*, both decreases the computational cost of the associated REMD-EVB simulations, and opens the door to more efficient studies of biochemical reactivity in systems with significant conformational fluctuations along the chemical reaction coordinate.

1. Introduction

Molecular dynamics (MD) simulations are commonly used to calculate the time evolution of various (bio)chemical systems, ranging in size from short-timescale simulations of atomic collisions *in vacuo* to μ -timescale simulations of large biomolecular systems. However, the complexity of the underlying energy landscapes and the long timescales of the processes involved remains a challenge [1]: molecular dynamics simulations typically use step sizes on the order of the fastest motion of the system. This is generally limited by bond-stretching and bending, and is on the order of 10^{-15} s, with specialized approaches such as hydrogen mass repartitioning allowing for timesteps of up to 4 fs [2]. However, most biochemical processes of interest take place on the millisecond timescale and beyond [3], putting many of them out of the

reach of conventional (unbiased) MD simulations. In addition, this means that the ergodicity principle might not be fulfilled for such systems, as a result of insufficient sampling due to too short simulation times [4]. Furthermore, insufficient sampling can cause MD trajectories to become trapped in the various local minima on the energy landscape, due to the large number of degrees of freedom in complex systems. Finally, trajectories can also get trapped in potential energy wells that are separated by high energy barriers [4].

A solution to this problem is the use of enhanced sampling approaches to improve the sampling of the energy surface. As outlined in Ref. [5], such methods largely fall into four classes: (I) path sampling techniques that focus on improving the sampling of transitions between two pre-defined states of the system, (II) tempering or generalized ensemble approaches, that enhance sampling by modifying the system

Abbreviations: 3D, three dimensional; CI, confidence interval; CPU, central processing unit; CV, collective variable; DFT, density functional theory; DHAP, dihydroxyacetone phosphate; DHFR, dihydrofolate reductase; EVB, empirical valence bond; FEP/US, free energy perturbation / umbrella sampling; GAP, α -glyceraldehyde-3-phosphate; MD, molecular dynamics; NUMA, non-uniform memory access; PRA, *N'*-(5'-phosphoribosyl)anthranilate; PriA, phosphoribosyl isomerase A; PTP1B, protein tyrosine phosphatase 1B; ProFAR, *N'*-[(5'-phosphoribosyl)formimino]-5-aminoimidazole-4-carboxamide ribonucleotide; QM/MM, quantum mechanics/molecular mechanics; REMD, replica exchange molecular dynamics; SCAAS, surface constrained all-atom solvent; TPI, triosephosphate isomerase.

* Corresponding author. School of Chemistry and Biochemistry, Georgia Institute of Technology, 901 Atlantic Drive NW, Atlanta, GA, 30332-0400, USA.

E-mail address: skamerlin3@gatech.edu (S.C.L. Kamerlin).

¹ Current address: Nimble Growth and Data AB, Sveavägen 66, 111 34 Stockholm, Sweden.

<https://doi.org/10.1016/j.jmglm.2022.108402>

Received 17 November 2022; Received in revised form 17 December 2022; Accepted 26 December 2022

Available online 30 December 2022

1093-3263/© 2023 The Authors. Published by Elsevier Inc. This is an open access article under the CC BY license (<http://creativecommons.org/licenses/by/4.0/>).

Hamiltonian to lower barrier heights, (III) decomposition techniques, and (IV) collective variable (CV) based biasing techniques [6–12]. Here, our focus is on the second of these, and in particular on replica exchange molecular dynamics (MD), which is a CV-independent advanced generalized ensemble sampling technique [13]. Many different flavors of this approach have been developed [1,14–19], however, at its core, REMD enhances the sampling of the system by running multiple replicas in parallel at different temperatures, and exchanging the temperature of non-interacting replicas at given intervals in order to overcome multiple-minima. As a CV-independent approach, REMD provides the benefit of not requiring prior knowledge of the system being studied (which would otherwise be a pre-requisite for the selection of an appropriate reaction coordinate) [20]. However, the computational cost of this approach, in terms of the number of replicas, and the sampling time needed for convergence, increases with the size of the system [21]. The key concept of REMD is that pairs of simulations are exchanged at pre-defined intervals, the most efficient being exchange between neighboring replicas, due to overlap of the potential energies being sampled [17]. The exchanges can, in turn, be conditional and unconditional. Conditional exchange requires a specific criterion to be met in order for an exchange to occur, whereas the latter exchanges without pre-defined criteria. A schematic of unconditional exchange, as used in the current work, is shown in Fig. 1.

In parallel to the ongoing advances in various enhanced sampling techniques for describing the conformational properties of biomolecular systems [5,18,22], there is also ever-increasing interest in using multi-scale approaches to describe chemical reactions in biological systems [23–25]. Here, Warshel's empirical valence bond (EVB) approach [26] provides a particularly powerful tool, as it can predict free energies for chemical reactions in a wide range of complex systems, often with chemical accuracy [27,28]. This approach has been described in detail elsewhere [26,28], but, in brief, it is a classical approach in which different force fields are parameterized to describe different chemical states of interest, and this is then transferred to a quantum mechanical valence-bond based framework by mixing these force fields using free energy perturbation/umbrella sampling (EVB-FEP/US). In the EVB approach, chemical reactivity is modelled by use of Morse potentials to describe the bonds that change along the reaction coordinate, as well as a Buckingham-type potential to describe van der Waals interactions between reacting atoms, and prevent system instabilities as bonds change along the reaction coordinate.

The advantages of using the EVB approach to model chemical reactivity are that well-parameterized force fields can reliably describe

thermodynamic properties of interest, while at the same time, as it is a classical approach at its core, this allows for greater conformational sampling than, for example, is possible using DFT-based QM/MM approaches (or approaches using higher levels of theory). In addition, EVB simulations are performed using an energy gap reaction coordinate, which is simply the energy between the two VB states being modelled ($\Delta\varepsilon = \varepsilon_1 - \varepsilon_2$, where ε_1 and ε_2 are the energies of the different VB states, Fig. 2). While there is a geometric component to these, as the energies of the individual states are based on the geometries of the structures in each of the VB states, the advantage of using the energy gap reaction coordinate, as opposed to a pure geometric reaction coordinate, is that it allows for the full multidimensional configurational space of the reacting system to be projected onto a single energy-based reaction coordinate [26,28]. This, in turn, accelerates the convergence of the free energy calculations [29].

Despite these advantages, it can be attractive to further improve the sampling of the dynamical properties of the system along the chemical reaction coordinate during EVB simulations, and, indeed, this was successfully done by Liu and Warshel in a study of dihydrofolate reductase (DHFR) [30], who used a protocol very similar to replica exchange to enhance the sampling of the hydride transfer catalyzed by this enzyme. Specifically, they performed their EVB-FEP/US simulations using 31 mapping windows (λ_m) of 180 ps in length, exchanging the system at adjacent frames every ps, performing the exchanges between frames (λ_1, λ_2) (λ_3, λ_4) ... ($\lambda_{29}, \lambda_{30}$) on odd swap cycles, and (λ_2, λ_3) (λ_4, λ_5) ... ($\lambda_{30}, \lambda_{31}$) on even swap cycles, in a similar alternating scheme as that used by the REMD implementation in GROMACS [31], as well as in prior replica exchange FEP/US approaches [32–34]. In replica exchange models that use conditional exchange between replicas, the use of an alternating model with exchanges between neighboring states is important for increasing the probability of each exchange attempt being successful, and reducing the frequency of unsuccessful exchanges [31].

This approach is formally similar to averaging the simulations over different initial conditions as well as running both EVB trajectories both backwards and forward between the different VB states, but allowed them to achieve this using a single 5.6 ns trajectory (31×180 ps) run in parallel, thus improving the sampling while simultaneously reducing the simulation time. We note that in this model, all exchanges between replicas are unconditional, expanding the accessible conformational space to the system during the simulations, with all exchanges between replicas accepted. That is in contrast to prior replica exchange FEP/US simulations [32–35], as well as Hamiltonian replica exchange [1,36], which use conditional exchange between replicas. The objective of the

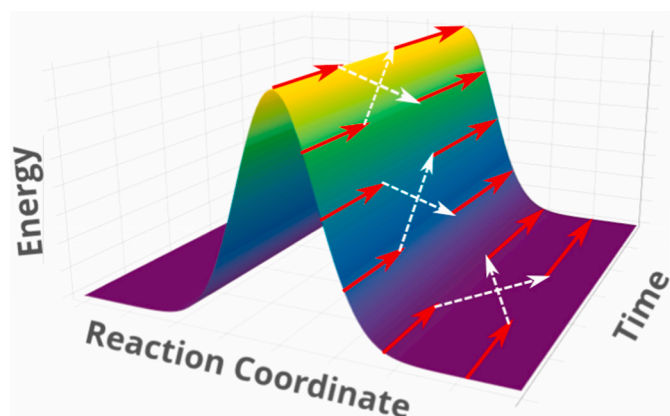


Fig. 1. Schematic representation of the unconditional exchange step on a 3D potential energy surface over time. Red lines indicate the individual umbrella sampling trajectories at different potential energies, white dashed arrows show the exchange step. All axes are in artificial units. (For interpretation of the references to colour in this figure legend, the reader is referred to the Web version of this article.)

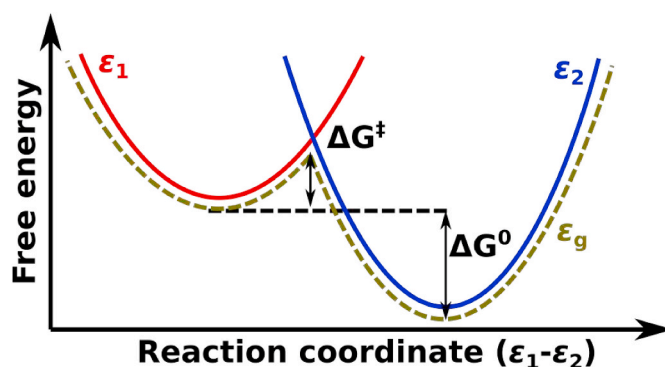


Fig. 2. Schematic representation of the empirical valence bond (EVB) framework, and the energy gap reaction coordinate [26,28]. The two diabatic VB states, ε_1 and ε_2 , are shown as red and blue solid lines, respectively. The adiabatic ground state free energy surface (ε_g) is shown as a green dashed line. The corresponding EVB activation free energy barrier (ΔG^\ddagger) and reaction free energy (ΔG^0) are labeled on the plot in black. (For interpretation of the references to colour in this figure legend, the reader is referred to the Web version of this article.)

FEP/US trajectory is to generate as many conformations as possible along the EVB reaction coordinate, defined by the mixing of the individual diabatic states defining the reaction coordinate, and the actual adiabatic ground state free energy surface is then obtained by matrix diagonalization, within a VB-based quantum mechanical framework [26,28]. This is important, as with all FEP calculations, the extent to which the conformational space can be sampled is the major criterion that limits the accuracy of the calculations [35], a problem that becomes more pronounced the more complex the system being studied is (for example simulations of biomolecular systems involving conformational plasticity along the chemical reaction coordinate).

Inspired by prior work [30], we have developed an open-source Python-based tool *Q-RepEx*, that interfaces with the Q6 simulation package [37], allowing for EVB-FEP/US simulations to be performed within a replica-exchange framework (REMD-EVB). We apply this approach to three model systems, studied by conventional EVB simulations in our prior work, triosephosphate isomerase from *Saccharomyces cerevisiae* (γ TPI) [38–40], PriA from *Mycobacterium tuberculosis* (MtPriA) [41], and protein tyrosine phosphatase 1B (PTP1B) [42,43], and demonstrate that this REMD-EVB framework significantly enhances conformational sampling while reducing computational cost (compared to the need to run a substantially larger number of replicas). *Q-RepEx* thus provides a useful tool for studies of chemical reactions in complex systems with significant conformational fluctuations along the chemical

reaction coordinate, where substantial conformational sampling is critical.

2. Methodology

Q-RepEx is an open-source Python tool, designed to perform replica exchange empirical valence bond (REMD-EVB) simulations using the Q6 simulation package [37]. The concept is adapted from Ref. [30], and the source code is available on GitHub at the following link: <https://github.com/kamerlinlab/Qrepex>, under the GNU General Public License version 2 (GPLv2), as well as on Zenodo, <https://doi.org/10.5281/zenodo.7331764>. The REMD-EVB procedure parallelizes the EVB-FEP/US calculations and thus increases and accelerates the sampling of the simulations, thus improving the statistics obtained. The main functionality of *Q-RepEx* is the unconditional exchange of simulation conditions for a series of EVB/FEP-US simulations.

The user provided input for *Q-RepEx* is purposely short in order to ease functionality. An example input is shown below:

```
1 python repex_v1.0.py fep_10 5 (3)
```

where *repex_v1.0.py* is the name of the current version of *Q-RepEx*, *fep_* is the base filename, 10 is the number of λ windows to use in the EVB-FEP/US simulation and 5 is the number of consecutive runs to be

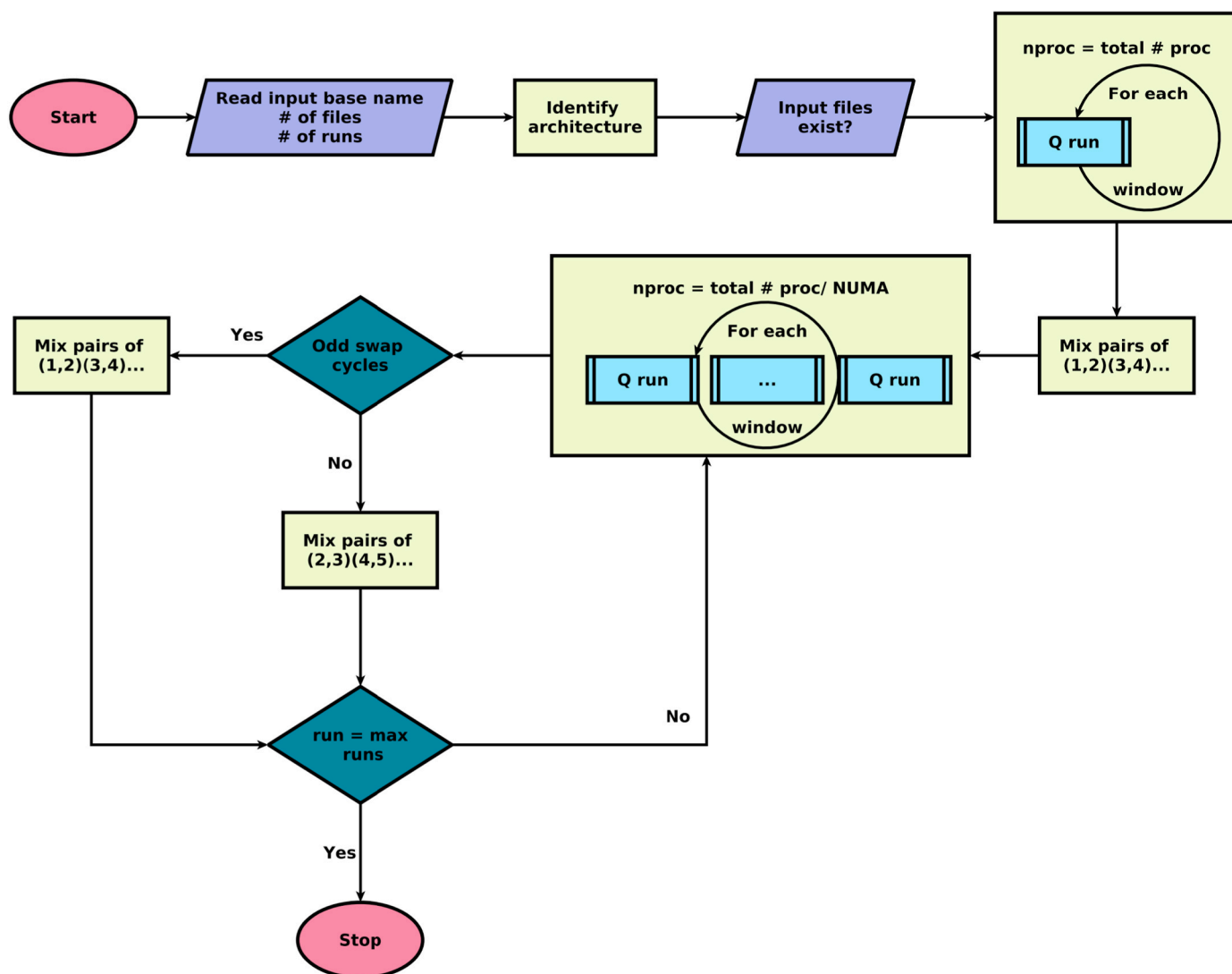


Fig. 3. Schematic overview of the *Q-RepEx* protocol. For details, see the main text.

performed. This can then be user modified to be adapted to the individual runs. The base filename has to be used for the input, output, trajectory, restart and energy files. The optional input (3) can be used for restarting *Q-RepEx* simulations from the 3rd run forward. A help module is provided in *Q-RepEx*. It can be activated by issuing the command:

```
2 python repex_v1.0.py help
```

A schematic representation of the *Q-RepEx* procedure is provided in Fig. 3. The user provided input is read in from the command line. The code then identifies the CPU architecture, which is later used to best parallelize the *Q6* runs. *Q-RepEx* checks for the existence of relevant input files before an initial, sequential run over all input files is performed. This is necessary for generating the initial restart files from each λ window. The *Q6* restart files contain coordinates and velocity information at each window. Exchanging these between different windows changes the initial conditions for each run. A first mixing of initial conditions occurs after the initial run over all FEP-US windows has completed. Subsequently, *Q-RepEx* enters a loop over the number of runs, where one *Q6* run is performed per available CPU socket, if more than one is available, otherwise all cores are used, until all files have finished.

Once all EVB-FEP/US windows have been simulated, on odd numbered runs, *Q-RepEx* exchanges restarts files in pairs, starting with the first window. On even numbered runs, the exchange is performed in pairs starting with the second restart file. As outlined in Ref. [30], this procedure is equivalent to averaging over various initial conditions. It therefore allows the reduction of the number of replicas required for sufficient sampling. Additionally, the exchange of simulation conditions in interchanging patterns for odd and even runs leads to a complete exchange of the starting conformations over the EVB/FEP-US reaction path. This is more efficient than the alternative of performing many forward and backward EVB-FEP/US simulations, in order to obtain adequate sampling of the system.

On most common computer clusters, each node consists of several CPU sockets, using NUMA architecture. In such architecture, CPU sockets are clustered into islands that host about one to two dozen cores. This corresponds to optimal performance of *Q6* parallelization. This approach allows for the replica-exchange EVB runs to be performed in parallel. While the increased amount of *Q6* executions inevitably increases the overhead, the speedup, due to running the EVB-FEP/US λ windows in parallel, does overall shorten the computation time.

The performance of *Q-RepEx* against conventional EVB simulations was tested on three reactions that we have studied extensively in prior work: the isomerization of substrate D-glyceraldehyde-3-phosphate (GAP) by triosephosphate isomerase from *Saccharomyces cerevisiae* (γ TPI) [38–40], the isomerization of substrate ProFAR by PriA from *Mycobacterium tuberculosis* (*MtPriA*) [41], and the rate-limiting hydrolysis of the phosphoenzyme intermediate formed during the reaction catalyzed by protein tyrosine phosphatase 1B (PTP1B) [42,43]. Here, we used the same system setup and starting structures as in prior studies for all three systems (PDB IDs 1NEY [44], 3ZS4 [45] and 3I80 [46] for γ TPI, *MtPriA* and PTP1B, respectively), as well as the EVB equilibration procedure outlined in detail in Ref. [41]. In the case of *MtPriA*, for simplicity, we selected 10 equilibration trajectories out of the 30 total generated for our prior work (selecting every third trajectory we ran) [41], and used these equilibration endpoints as the starting points for our various *Q-RepEx* simulations. As PriA is a bi-functional enzyme, we used here PDB ID: 3ZS4 [45], which has loop 5 of PriA in a “pro-ProFAR” conformation necessary for catalyzing the substrate studied here (see discussion in e.g. Refs. [41,47]). In the case of γ TPI [38,39] and PTP1B [42,43], as there were slight differences in the equilibration procedure used for those works and our *MtPriA* study [41], we generated 10 new equilibrated trajectories using the protocol described for PriA in Ref. [41], and used these as starting points for our various REMD-EVB calculations, using PDB ID: 1NEY [44] (*Saccharomyces cerevisiae* TPI in

complex with substrate dihydroxyacetone phosphate) as our starting point. The root mean square deviations (RMSD) of all backbone atoms during our respective equilibration runs is shown in Fig. S1.

All simulations were performed using the OPLS-AA force field [48], with the protein immersed in a droplet of either 25 (TPI), 30 (PriA) or 22.5 Å (PTP1B) radius of TIP3P water molecules [49], described using the surface constrained all-atom solvent (SCAAS) model [50]. The reacting region was described using the same valence bond states and EVB parameters as in prior work. For each system, we performed six individual sets of REMD-EVB simulations: 5 runs of 10 ps length per λ window (5×10), 5 runs of 20 ps length per λ window (5×20), 10 runs of 10 ps length per λ window (10×10), 10 runs of 20 ps length per λ window (10×20), 10 runs of 100 ps length per λ window (10×100), and 10 runs of 200 ps length per λ window (10×200). This leads to total simulation times of 25.5 ns for our (5×10), 51 ns for our (5×20), 51 ns for our (10×10), 102 ns for our (10×20), 510 ns for our (10×100) and 1020 ns for our (10×200) runs over 10 replicas. We also performed conventional EVB simulations 51×20 ps (with a total simulated time of 10.2 ns) and 51×200 ps (with a total simulated time of 102 ns) runs per replica, again 10 replicas for comparison, using the same initial equilibration runs as for the REMD-EVB runs. All energy analysis was performed using the *Qfep* module of the *Q6* software package [37]. For further simulation details, see Refs. [26,37,51].

Bootstrapping with replacement is a statistical technique which enables one to estimate summary statistics for a dataset. Here, we used bootstrapping to generate probability densities representing the distribution of the calculated ΔG^\ddagger and ΔG_0 values obtained from our simulations for the six different sampling protocols investigated for each system. We note that bootstrapping was performed on the already determined raw ΔG^\ddagger and ΔG_0 values (described above), essentially treating them as observations, and not as a way to post-process the EVB simulations. For each sampling protocol and system, we performed 5000 bootstrap resamples on the calculated ΔG^\ddagger and ΔG_0 values (separately) to generate 5000 average ΔG^\ddagger and ΔG_0 values. These 5000 bootstrapped averaged values obtained for each scenario and system were then converted to probability densities using a Gaussian kernel density estimation with 25 equally spaced bins. The lower and upper boundary range for the probability densities was kept consistent for each system and was determined by the minimum and maximum bootstrap sample value obtained for any of the six scenarios for that given system.

Random subsampling was performed on the 10×10 and 10×20 protocols in order to generate 95% confidence intervals (CIs) for a varying number of replicas. Random subsampling is a modified form of bootstrapping in which less observations (*i.e.*, replicas) are used to generate each resample of the data. This allows one to predict how a differing number of replicas would impact the precision of the results obtained. Random subsampling was performed using replica ranges of 1–10, with resampling performed 5000 times in order to calculate the average values and the 95% CIs. The upper and lower bounds of the 95% CIs were determined by taking the 125th (2.5%) and 4875th (97.5%) values of the rank-ordered average ΔG_0 and ΔG^\ddagger values obtained from the 5000 resamples per dataset.

3. Results and discussion

In order to compare the performance of *Q-RepEx* against conventional EVB simulations, we applied the *Q-RepEx* protocol shown in Fig. 3 to three previously studied enzymes. The first of these (Fig. S2), triosephosphate isomerase (TPI), is a tremendously proficient catalyst of the reversible isomerization of D-glyceraldehyde-3-phosphate (GAP) to dihydroxyacetone phosphate (DHAP). TPI is activated by a large ligand-gated conformational change, in which a key catalytic loop, loop 6, moves ~ 7 Å from a catalytically inactive open conformation to a catalytically active closed conformation, thus closing over the active site and sequestering it from solvent [52,53]. Loop closure over the active site elevates the pK_a of a key catalytic glutamic acid (estimated to be as high

as ~ 10 in the presence of trianionic phosphoglycolate [54]), which, in turn, allows this side chain to deprotonate the substrate. This initial proton transfer step is expected to be rate-limiting, with subsequent steps in the isomerization to be fast in comparison to the initial proton transfer, and thus the initial substrate deprotonation has been the focus of our prior EVB simulations of wild-type and variant forms of TPis from a range of different organisms, with good agreement with experiment

[40]. Here, we use the initial deprotonation of substrate DHAP as catalyzed by wild-type TPI from *Saccharomyces cerevisiae* (γ TPI) as a model reaction for evaluating the performance of *Q-RepEx*.

The second of these, PriA (Fig. S3) from *Mycobacterium tuberculosis* (*MtPriA*), is also a TIM-barrel fold protein, and is a promiscuous catalyst of the Amadori rearrangements leading to the isomerization of substrates ProFAR and PRA by this enzyme. Our focus here is on the first

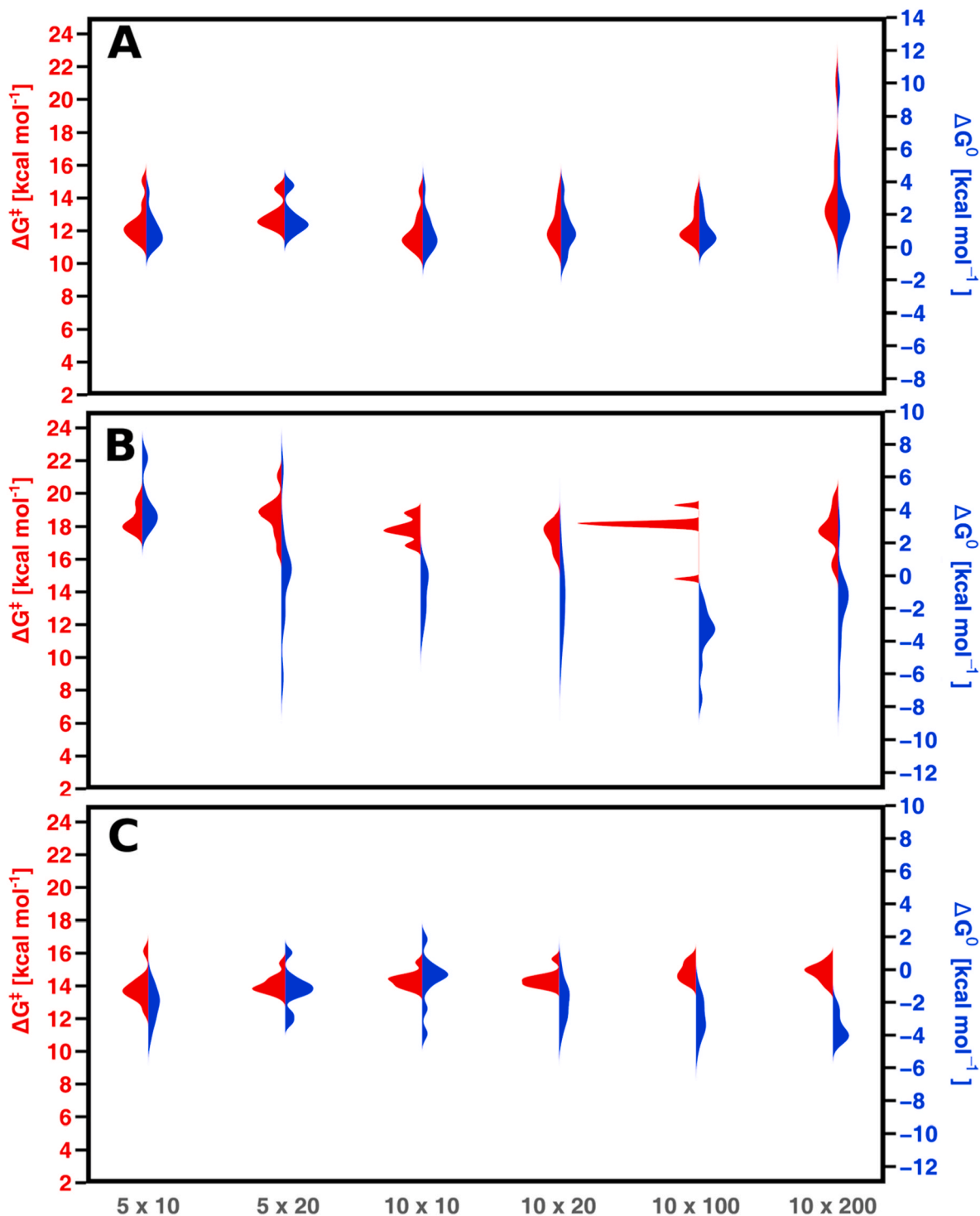


Fig. 4. The density of the free energy barriers (ΔG^\ddagger , red) and the density of the ΔG_0 (blue) of the six different sets of *Q-RepEx*. Shown here are calculated free energies from REMD-EVB simulations of (A) γ TPI, (B) *MtPriA* and (C) PTP1B. The x-axis labels 5×10 , 5×20 , 10×10 , 10×20 , 10×100 , and 10×200 correspond to REMD-EVB sampling performed in 5 runs of 10 ps, 5 runs of 20 ps, 10 runs of 10 ps, 10 runs of 20 ps, 10 runs of 100 ps, and 10 runs of 200 ps with 10 starting conformations. All simulations were performed using 51 individual λ windows per trajectory, and 10 independent starting conformations per system. (For interpretation of the references to colour in this figure legend, the reader is referred to the Web version of this article.)

step of this isomerization process, *i.e.* the ring-opening of substrate ProFAR (the first step of the mechanism shown in Fig. S3), following our prior work [41]. Similarly to TPI, PriA also has a number of long loops decorating the active site, the conformational distribution of which is important for determining selectivity and activity [41,47]. As discussed in detail elsewhere [41,47], one of these loops, loop 5, alternates between a knot-like “pro-ProFAR” and a β -hairpin “pro-PRA” conformation of the loop, depending on which substrate is being catalyzed. Here, we are starting from a structure of loop 5 in a pro-ProFAR conformation, as described in the **Methodology** section.

Finally, PTP1B (Fig. S4) is a protein tyrosine phosphatase (PTP) that plays an important role in the regulation of signal transduction [55], and is a major drug target for treating type 2 diabetes and obesity [55–57], and a major cancer therapeutic target [58]. This enzyme catalyzes a two-step cleavage/hydrolysis mechanism, in which an active site cysteine first acts as a nucleophile attacking the phosphate group of the substrate, followed by rate-limiting hydrolysis of the resulting phospho-cysteine intermediate, with involvement of an aspartic acid located on a mobile loop, the WPD-loop, in acid-base catalysis [59]. As with TPI, the WPD-loop undergoes a substantial conformational change from a catalytically active loop-open to a catalytically-active loop-closed conformation to position the aspartic acid side chain in an optimal position for catalysis [60]. The dynamical behavior of this loop has been suggested by both experimental and computational work to be important for determining the activity of PTPs more broadly [42,43,61–65]. Taken together, the three systems studied here cover a span of chemical reactions, isomerization, ring-opening, and phosphoryl transfer, against which to test the performance of *Q-RepEx*.

Our prior EVB simulations of all three systems [38–43] were performed using 30 individual starting structures (endpoints of 30 individual equilibration runs initiated with different random velocities), with the EVB-FEP/US simulations performed over 51 λ windows of 200 ps/length per window (*i.e.* 10.2 ns/trajectory, cumulative 306 ns over 30 trajectories per system). We have repeated these simulations in the present work to ensure consistent protocols, using 10 replicas per system, based on the same initial equilibration endpoints as for our REMD-EVB simulations. Our REMD-EVB simulations were performed using up to 10 starting conformations, again using 51 λ windows per trajectory. Following from this, six individual sets of REMD-EVB simulations of increasing simulation lengths were performed as described in the **Methodology** section. The results of these simulations are summarized in Tables 1 and S1, and Fig. 4.

From Table 1, it can be seen that for all systems modelled here, the calculated values are within 1.5 kcal mol⁻¹ deviation at most from the corresponding experimental values, with similar standard error of the mean on the calculated activation free energies from the conventional and replica-exchange EVB simulations. When looking at the distribution of the calculated activation and reaction free energies (Fig. 4) across the different systems and simulation lengths, it can be seen that there is no clear trend in either activation or reaction free energies across different systems and simulation times, but all values typically fall within a relatively narrow energetic range of ± 0.6 kcal mol⁻¹, occasionally with longer tails on the distribution. The average values remain stable across the different simulations. However, in the case of the reaction free energy, ΔG_0 (Table S1), it appears that increasing simulation time can affect average calculated ΔG_0 by several kcal mol⁻¹, and therefore the additional sampling time becomes important, in particular for multi-step reactions where the energetics of each subsequent step are dependent on correctly calculating the reaction free energy of the prior step.

We are also interested in the impact of our REMD-EVB simulations on average execution time per trajectory and simulation length, compared to our conventional EVB simulations. This data is summarized in Table 2, with all simulations being performed on two 32-core Intel Xeon Gold 6130 CPUs. From this table, it can be seen that a single conventional EVB trajectory of a length that is typically adequate to obtain convergent simulations, as in our prior work [38,40–43,67], takes

Table 1

A comparison of experimental and calculated activation free energies (ΔG^\ddagger), with the calculated values obtained using conventional EVB simulations, or REMD-EVB simulations of varying lengths.^a

Simulation Setup	Total Simulation Time	γ TPI	MtPriA	PTP1B
$\Delta G_{\text{exp}}^\ddagger$		12.9 [66]	18.3 [47]	14.3 [59]
$\Delta G_{\text{EVB}}^\ddagger$				
20	10.2	12.0 \pm 0.9	18.1 \pm 0.4	14.6 \pm 0.4
200	102	12.5 \pm 0.9	18.0 \pm 0.3	14.3 \pm 0.2
$\Delta G_{\text{REMD-EVB}}^\ddagger$				
5 \times 10	25.5	11.5 \pm 0.6	17.9 \pm 0.5	13.7 \pm 0.5
5 \times 20	51	11.9 \pm 0.7	18.6 \pm 0.6	13.9 \pm 0.3
10 \times 10	51	11.7 \pm 0.6	17.8 \pm 0.3	14.2 \pm 0.3
10 \times 20	102	12.1 \pm 0.6	17.7 \pm 0.4	14.1 \pm 0.2
10 \times 100	510	13.3 \pm 1.3	18.0 \pm 0.4	14.7 \pm 0.4
10 \times 200	1020	12.8 \pm 0.5	17.8 \pm 0.6	14.9 \pm 0.3

^a All energies are shown in kcal mol⁻¹, simulation setup timescales for each individual window in ps, and total simulation times in ns cumulative over all replicas per system. The experimental activation free energies, $\Delta G_{\text{exp}}^\ddagger$, were derived from experimentally measured k_{cat} values (presented in Refs. [47,59,66]), using transition state theory. The calculated activation free energies from conventional EVB simulations ($\Delta G_{\text{EVB}}^\ddagger$) are presented as averages and standard error of the mean over 10 individual conventional EVB trajectories, that were simulated as 51 individual λ windows of 20 and 200 ps/length, per trajectory. Our REMD-EVB simulations ($\Delta G_{\text{REMD-EVB}}^\ddagger$) were performed in six different lengths, again all using 51 individual λ windows: 5 \times 10, 5 \times 20, 10 \times 10, 10 \times 20, 10 \times 100, and 10 \times 200 correspond to sampling collected in 5 runs of 10 ps, 5 runs of 20 ps, 10 runs of 10 ps, 10 runs of 20 ps, 10 runs of 100 ps, and 10 runs of 200 ps with 10 starting conformations, and are again presented as average values and standard error of the mean over all trajectories. The corresponding data for the calculated reaction free energies is shown in Table S1.

approximately 30–40 h to execute using this architecture, for the systems studied in this work (10x longer than the shorter 20 ps/window simulations for each system). The difference in time to a REMD-EVB simulation of the corresponding length (*e.g.* our 10 \times 20 runs) might not seem large: only between 1.5 and 2.3-fold reduction in compute time. However, even this seemingly small difference becomes significant on longer simulation timescales: extrapolating our conventional EVB simulations to \sim 100ns/trajectory timescales (the longest REMD-EVB simulations performed in this work), the difference in human time per trajectory is substantive. Furthermore, it is possible to further enhance the sampling of the REMD-EVB simulations by changing the number of exchanges and replicas. Thus, while the REMD-EVB simulations do not necessarily provide a significant advantage for shorter simulation timescales, they make substantially longer simulation timescales per trajectory computationally tractable in terms of human time, which allows for the capturing of, for instance, more significant conformational fluctuations along the chemical reaction coordinate that is possible using conventional EVB or higher precision QM/MM approaches. Finally, our REMD-EVB approach provides improved sampling of conformational space compared to a conventional EVB simulation of the same length.

In order to evaluate the convergence of the different REMD-EVB protocols tested herein we turned to the statistical method of bootstrapping with replacement. Bootstrapping with replacement is a resampling procedure that generates many resamples of a given dataset of observations (in our case the individual ΔG^\ddagger and ΔG_0 values), with it being possible to have multiple repeats of a single observation in a bootstrap sample. For each sampling protocol and system, we generated

Table 2

Average per replica (human) compute time for conventional and replica-exchange simulations of various lengths for the three systems studied in this work.^a

Simulation Setup	Simulation Time/Trajectory	yTPI	MtPriA	PTP1B
$\Delta G_{\text{EVB}}^{\ddagger}$				
20	1.2	3.9 ± 0.1	4.2 ± 0.1	3.0 ± 0.0
200	10.2	38.6 ± 0.5	41.5 ± 0.9	32.4 ± 0.4
$\Delta G_{\text{REMD-EVB}}^{\ddagger}$				
5 × 10	2.55	6.0 ± 0.1	7.3 ± 0.1	3.9 ± 0.04
5 × 20	5.1	11.8 ± 0.1	14.5 ± 0.2	7.1 ± 0.1
10 × 10	5.1	11.2 ± 0.2	13.8 ± 0.3	7.1 ± 0.1
10 × 20	10.2	22.2 ± 1.0	27.5 ± 0.5	14.2 ± 0.4
10 × 100	51	111.0 ± 2.8	136.1 ± 1.1	70.4 ± 1.2
10 × 200	102	220.4 ± 3.9	279.2 ± 4.6	137.5 ± 2.6

^a All simulation times are shown in ns, and the per replica human compute time in hours. The latter are shown as averages and standard deviations over 10 individual trajectories per system and simulation length. Simulation setup timescales for each individual window in ps, and total simulation times in ns cumulative over all replicas per system. Conventional EVB trajectories were simulated as 51 individual λ windows of 20 and 200 ps/length, per trajectory REMD-EVB trajectories were performed in six different lengths, again all using 51 individual λ windows: 5 × 10, 5 × 20, 10 × 10, 10 × 20, 10 × 100, and 10 × 200 correspond to sampling collected in 5 runs of 10 ps, 5 runs of 20 ps, 10 runs of 10 ps, 10 runs of 20 ps, 10 runs of 100 ps, and 10 runs of 200 ps. All simulations were performed using 10 starting conformations, on two 32-core Intel Xeon Gold 6130 CPUs per trajectory.

5000 bootstrap resamples of the ΔG^{\ddagger} and ΔG_0 values (separately) and used this to calculate new ΔG^{\ddagger} and ΔG_0 average values. These averages were used to calculate probability densities for the calculated activation (ΔG^{\ddagger} , Fig. 5) and reaction (ΔG_0 , Fig. S5) free energies for each REMD-EVB simulation set. Note that the 10 × 100 run for yTPI is an outlier in this analysis, due to loop 6 opening in some of the replicas (a problem we have discussed at length in prior work [39]). From this data, it can be seen that the energy distributions fall in a narrow and overlapping range irrespective of simulation length. However, increasing the sampling time affects the distribution of the reaction free energies (Fig. S5), and also the calculated activation free energies in the case of PTP1B, and therefore the longer sampling times made accessible by *Q-RepEx* are

beneficial.

In order to quantify the bootstrapping results, we determined the 95% confidence intervals (CIs) which are provided in full in Tables S3 and S4. By calculating the range between the lower and upper bounds of the CIs obtained for each system and sampling strategy, we identified the 10 × 10 and 10 × 20 strategy to provide a narrow range of ΔG^{\ddagger} values for each system, see Table S3. For example, the ranges between the lower and upper bound for these 2 strategies for each system is ~1 kcal mol⁻¹ for PTP1B, between 1.2 and 1.9 kcal mol⁻¹ for MtPriA and 2.1–2.2 kcal mol⁻¹ for yTPI, Table S3. Further and as observed in the probability densities (Fig. 5), the longer sampling procedures can give rise to erroneous results as seen in yTPI's 10 × 100 procedure (due to loop opening events), and in all 3 systems the increased sampling had no notable improvement on the confidence interval ranges (Table S3). On this basis, the longer sampling strategies are likely to be unnecessary as they do not increase precision and of course, require substantially more compute time.

Our bootstrapping results described above indicated the 10 × 10 and 10 × 20 protocols to consistently provide a good balance of precision and low compute resources when calculating the activation free energies. In the following section we therefore focused on these two protocols and applied random sub sampling to evaluate how the number of replicas used would be expected to alter the 95% CIs of the results obtained for each enzyme. Random subsampling is a variant of bootstrapping with replacement whereby each resample of the data is made up of less observations than the total distribution, which in this case allowed us to predict the extent to which the CIs would reduce as more and more observations/repeats are used per sample. The results from our random subsampling analysis on the calculated ΔG^{\ddagger} are shown in Fig. 6 and on the calculated ΔG_0 are shown in Fig. S6. We note that the average value from each subsample is the product of 5000 resamples of the dataset and therefore would not be expected to alter with changing numbers of replicas. Across all 3 systems and replicas, the 95% CIs show a similar pattern in which increasing replicas leads to improved precision, and after approx. 5 replicas per system the change in CIs becomes rather small (Fig. 6). For example, 1 replica in PTP1B has a range between the lower and upper bound of the 95% CIs of 3.3 kcal mol⁻¹, which decreases to 1.3 kcal mol⁻¹ after 5 replicas and then to 1.0 kcal mol⁻¹ after 10 replicas in the 10 × 20 protocol. Likewise, this observation is also borne out in MtPriA, with 1 replica giving a range between 6 kcal mol⁻¹, which decreases to 2.6 kcal mol⁻¹ after 5 replicas and then to 1.9 kcal mol⁻¹ after 10 replicas. Finally, 1 replica gives a range of 7.1 kcal mol⁻¹, which decreases to 3.1 kcal mol⁻¹ after 5 replicas and then to 2.2 kcal mol⁻¹ after 10 replicas. Given the above observations, it could be reasonable to perform 5 replicas instead of 10 in situations

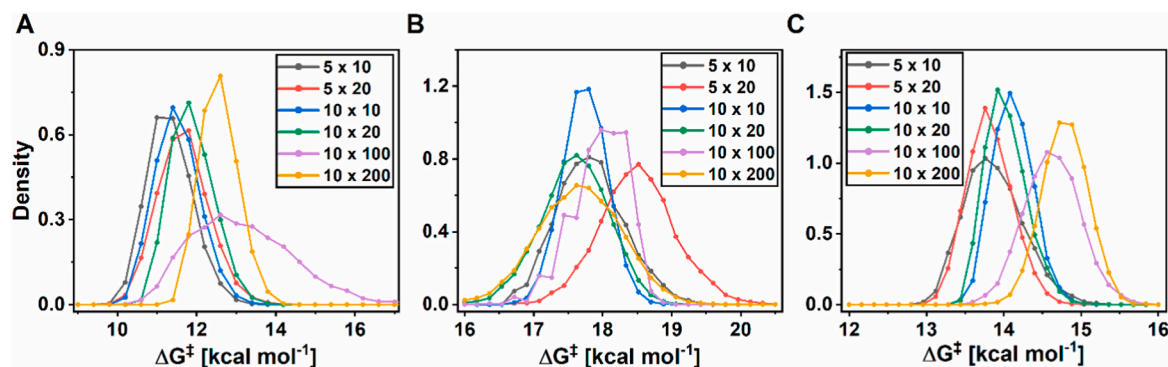


Fig. 5. Bootstrapping analysis performed on the calculated reaction free energies (ΔG^{\ddagger}) of the REMD-EVB simulations of (A) yTPI, (B) MtPriA and (C) PTP1B. The legends 5 × 10, 5 × 20, 10 × 10, 10 × 20, 10 × 100, and 10 × 200 correspond to sampling collected in 5 runs of 10 ps, 5 runs of 20 ps, 10 runs of 10 ps, 10 runs of 20 ps, 10 runs of 100 ps, and 10 runs of 200 ps with 10 starting conformations per system and simulation time. Probability distributions of the calculated ΔG^{\ddagger} values obtained from performing bootstrapping with replacement (5000 bootstrap resamples). The probability densities were generated using a Gaussian kernel density estimation on the ΔG^{\ddagger} values obtained from each bootstrap sample and provide a way to visualize the possible distribution of results obtained for each sampling protocol. Equivalent results for the calculated ΔG_0 values are provided in Fig. S5.

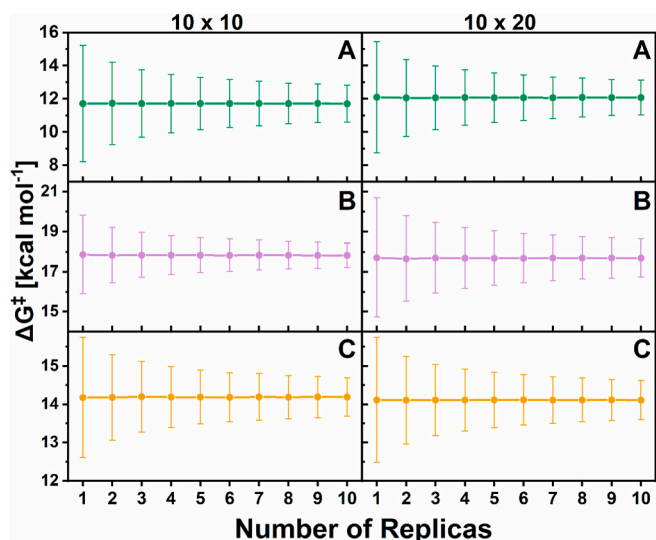


Fig. 6. Results from random subsampling calculations performed on the calculated activation free energies (ΔG^\ddagger) of the REMD-EVB simulations of (A) yTPI, (B) MtPriA and (C) PTP1B for the 10×10 and 10×20 protocols. Random subsampling was used to investigate how the 95% confidence intervals (the error bars on each plot) are impacted by how many replicas were used in the random subsampling. Note that as the average ΔG^\ddagger values are made up of 5000 subsamples, they are not expected to change with an increasing number of replicas. Equivalent results for the calculated reaction free energies (ΔG_0) are provided in Fig. S6.

where high throughput screening of many variants is required and/or compute resources are limited. Regardless, our subsampling results clearly demonstrate the needs for repeats in order to generate precise predictions of ΔG^\ddagger for all three model systems.

By comparing the bootstrapping and random subsampling results obtained for the ΔG^\ddagger (Fig. 6 and Table S3) and ΔG_0 values (Fig. S6 and Table S4), one can clearly identify that CI ranges are notably larger for the ΔG_0 values. For example, for the two protocols selected, the CI ranges (the difference between the lower and upper bounds) for the ΔG_0 values are between 2.2 and 5.2 kcal mol⁻¹ (Table S4), compared to between 1.0 and 2.2 kcal mol⁻¹ for the ΔG^\ddagger values (Table S3). This is likely because the transition state (TS) is more rigidly defined, and therefore samples a narrower distributions of values making it easier to converge (when compared to the product state). These observations are important to consider because when studying a single step reaction, a confident estimate of the ΔG_0 values may not be important, if determining ΔG^\ddagger is the primary goal. However, in cases where the reaction is multi-step, more replicas may be required to converge the ΔG_0 values (as the product state of the proceeding step will act as the reactant state for the next step and therefore impact the calculated ΔG^\ddagger values). That said, by using the bootstrapping/random subsampling protocol demonstrated herein, one can readily assess if more replicas would need to be run or not.

4. Conclusions

In order to calculate highly accurate free energy profiles of chemical and biochemical reactions efficient and sufficient sampling of the PES is required. EVB-FEP/US simulations follow a reaction path in time. The US enables the simulation to overcome high barriers along the reaction path. However, the necessity to perform these calculations sequentially slows down these simulations of biochemical reactions. Additionally, a large number of replicas, starting from different starting conformations, as well as ideally forward and backward EVB-FEP/US runs are required to sufficiently sample the PES. The Python pipeline *Q-RepEx*, presented here, allows for more efficient sampling of (bio)chemical reactions using

the *Q6* software package [37]. The unconditional replica-exchange mechanism used by *Q-RepEx* reduces the amount of replicas required. Furthermore, it allows for the EVB simulations of the chemical reactions of interest (irrespective of the environment the reaction is simulated in Ref. [68], whether in vacuum, solvent or e.g. a protein active site) to be performed in parallel. The interchanging exchange steps lead to a mixing of starting conformations which increases sampling, and thus boosts performance. Therefore, *Q-RepEx* can be used to extend EVB simulations to larger and more complex systems, the computational cost of which would prohibit such studies using conventional EVB simulations. Finally, while the current implementation of *Q-RepEx* is interfaced with *Q6*, the flowchart shown in Fig. 3 can easily be extended to other computational toolkits with minimal modifications.

Code availability

The *Q-RepEx* script is available free of charge on GitHub at <https://github.com/kamerlinlab/Qrepex> and Zenodo at <https://doi.org/10.5281/zenodo.7331764>. It depends on NUMP, MPI and *Q6* (which is, in turn, available for download from GitHub at <https://github.com/quers/Q6>).

Funding

This work was supported by the Knut and Alice Wallenberg Foundation [grant numbers 2018.0140, 2019.0431], and the Swedish Research Council [grant number 2019-03499]. The computations were enabled by resources provided by the Swedish National Infrastructure for Computing (SNIC), partially funded by the Swedish Research Council through grant agreement no. 2018-05973.

Declaration of competing interest

The authors declare that they have no known competing financial interests or personal relationships that could have appeared to influence the work reported in this paper.

Acknowledgements

The authors thank Profs. Arie Warshel and Peter Kasson for valuable discussion.

Appendix A. Supplementary data

Supplementary data to this article can be found online at <https://doi.org/10.1016/j.jmgn.2022.108402>.

References

- [1] G. Bussi, Hamiltonian replica exchange in GROMACS: a flexible implementation, *Mol. Phys.* 112 (2014) 379–384.
- [2] C. Balusek, H. Hwang, C.H. Lau, K. Lundquist, A. Hazel, A. Pavlova, et al., Accelerating membrane simulations with hydrogen mass repartitioning, *J. Chem. Theor. Comput.* 15 (2019) 4673–4686.
- [3] D.A. Golombek, I.L. Bussi, P.V. Agostino, Minutes, days and years: molecular interactions among different scales of biological timing, *Philos. Trans. R. Soc. Lond. B Biol. Sci.* 369 (2014), 20120465.
- [4] A. Barducci, M. Bonomi, M. Parrinello, *Metadynamics*. Wiley Interdiscip. Rev. Comput. Mol. Sci. 1 (2011) 826–843.
- [5] H. Sidky, W. Chen, A.L. Ferguson, Machine learning for collective variable discovery and enhanced sampling in biomolecular simulation, *Mol. Phys.* 118 (2020), e1737742.
- [6] C. Chipot, A. Pohorille, *Free Energy Calculations*, Springer, Berlin, 2007.
- [7] E.E. Borrero, F.A. Escobedo, Reaction coordinates and transition pathways of rare events via forward flux sampling, *J. Chem. Phys.* 127 (2007), 164101.
- [8] R.J. Allen, C. Valeriani, P.R. ten Wolde, Forward flux sampling for rare event simulations, *J. Phys. Condens. Matter* 21 (2009), 463102.
- [9] C. Abrams, G. Bussi, Enhanced sampling in molecular dynamics using metadynamics, replica-exchange, and temperature-acceleration, *Entropy* 16 (2014) 163–199.

- [10] Y. Miao, J.A. McCammon, Unconstrained enhanced sampling for free energy calculations of biomolecules: a review, *Mol. Simulat.* 42 (2016) 1046–1055.
- [11] B.E. Husic, V.S. Pande, Markov state models: from an art to a science, *J. Am. Chem. Soc.* 140 (2018) 2386–2396.
- [12] C. Wehmeyer, M.K. Scherer, T. Hempel, B.E. Husic, S. Olsson, F. Noé, Introduction to markov state modeling with the PyEMMA software, *LiveComS 1* (2019) 5965.
- [13] Y. Sugita, Y. Okamoto, Replica-exchange molecular dynamics method for protein folding, *Chem. Phys. Lett.* 314 (1999) 141–151.
- [14] Y.M. Rhee, V.S. Pande, Multiplexed-replica exchange molecular dynamics method for protein folding simulation, *Biophys. J.* 84 (2003) 775–786.
- [15] R. Zhou, *Replica Exchange Molecular Dynamics Method for Protein Folding Simulations*, Humana Press, New York, NY, 2007.
- [16] J.D. Chodera, M.R. Shirts, Replica exchange and expanded ensemble simulations as gibbs sampling: simple improvements for enhanced mixing, *J. Chem. Phys.* 135 (2011), 194110.
- [17] M. Meli, G. Colombo, A Hamiltonian replica exchange molecular dynamics (MD) method for the study of folding, based on the analysis of the stabilization determinants of proteins, *Int. J. Mol. Sci.* 14 (2013) 12157–12169.
- [18] R.C. Bernardi, M.C.R. Melo, K. Schulten, Enhanced sampling techniques in molecular dynamics simulations of biological systems, *Biochim. Biophys. Acta* 1850 (2015) 872–877.
- [19] Y. Sugita, M. Kamiya, H. Oshima, S. Re, *Replica-Exchange Methods for Biomolecular Simulations*, Humana, Springer Nature, New York, N. Y., 2022.
- [20] R. Petraglia, A. Nicolai, M.D. Wodrich, M. Ceriotti, C. Corminbeuf, Beyond static structures: putting forth REMD as a tool to solve problems in computational organic chemistry, *J. Comput. Chem.* 37 (2016) 83–92.
- [21] N. Rahore, M. Chopra, J.J. de Pablo, Optimal allocation of replicas in parallel tempering simulations, *J. Chem. Phys.* 122 (2005) 2411.
- [22] Y.I. Yang, Q. Shao, J. Zhang, L. Yang, Y.Q. Gao, Enhanced sampling in molecular dynamics, *J. Chem. Phys.* 151 (2019), 070902.
- [23] U. Ryde, QM/MM calculations on proteins, *Methods Enzymol.* 577 (2016) 119–158.
- [24] J. Ainsley, A. Lodola, A.J. Mulholland, C.Z. Christov, T.G. Karabencheva-Christova, Combined quantum mechanics and molecular mechanics studies of enzymatic reaction mechanisms, *Adv. Protein Chem. Struct. Biol.* 113 (2018) 1–32.
- [25] D.J. Huggins, P.C. Biggin, M.A. Dämgen, J.W. Essex, S.A. Harris, R.H. Henchman, et al., Biomolecular simulations: from dynamics and mechanisms to computational assays of biological activity, *WIREs Comp. Mol. Sci.* 9 (2018) e1393.
- [26] A. Warshel, R.M. Weiss, An empirical valence bond approach for comparing reactions in solutions and in enzymes, *J. Am. Chem. Soc.* 102 (1980) 6218–6226.
- [27] A. Warshel, P.K. Sharma, M. Kato, Y. Xiang, H. Liu, M.H.M. Olsson, Electrostatic basis for enzyme catalysis, *Chem. Rev.* 106 (2006) 3210–3235.
- [28] A. Shurki, E. Derat, A. Barrozo, S.C.L. Kamerlin, How valence bond theory can help you understand your (Bio)Chemical reaction, *Chem. Soc. Rev.* 44 (2015) 1037–1052.
- [29] L. Mones, P. Kulhánek, I. Simon, A. Laio, M. Fuxreiter, The energy gap as a universal reaction coordinate for the simulation of chemical reactions, *J. Phys. Chem. B* 113 (2009) 7867–7873.
- [30] H. Liu, A. Warshel, The catalytic effect of dihydrofolate reductase and its mutants is determined by reorganization energies, *Biochemistry* 46 (2007) 6011–6025.
- [31] M.J. Abraham, J.E. Gready, Ensuring mixing efficiency of replica-exchange molecular dynamics simulations, *J. Chem. Theor. Comput.* 4 (2008) 1119–1128.
- [32] W. Jiang, M. Hodoseck, B. Roux, Computation of absolute hydration and binding free energy with free energy perturbation distributed replica-exchange molecular dynamics, *J. Chem. Theor. Comput.* 5 (2009) 2583–2588.
- [33] W. Jiang, B. Roux, Free Energy Perturbation Hamiltonian Replica-Exchange Molecular Dynamics (FEP/H-REMD) for Absolute Ligand Binding Free Energy Calculations, vol. 6, 2010, pp. 2559–2565.
- [34] D. Min, H. Li, Synergistic approach to improve “alchemical” free energy calculation in rugged energy surface, *J. Chem. Phys.* 126 (2007), 144109.
- [35] L. Wang, B.J. Berne, R.A. Friesner, On achieving high accuracy and reliability in the calculation of reactive protein-ligand binding affinities, *Proc. Natl. Acad. Sci. U. S. A.* 109 (2012) 1937–1942.
- [36] H. Fukunishi, On the Hamiltonian replica exchange method for efficient sampling of biomolecular systems: application to protein structure prediction, *J. Chem. Phys.* 116 (2002) 9058.
- [37] P. Bauer, A. Barrozo, M. Purg, B.A. Amrein, M. Esguerra, P.B. Wilson, et al., Q6: a comprehensive toolkit for empirical valence bond and related free energy calculations, *Software* 7 (2018) 388–395.
- [38] Y.S. Kulkarni, Q. Liao, D. Petrovic, D.M. Krüger, B. Strodel, T.L. Amyes, et al., Enzyme architecture: modeling the operation of a hydrophobic clamp in catalysis by triosephosphate isomerase, *J. Am. Chem. Soc.* 139 (2017) 10514–10525.
- [39] Q. Liao, Y. Kulkarni, U. Sengupta, D. Petrovic, A.J. Mulholland, M. van der Kamp, et al., Loop motion in triosephosphate isomerase is not a simple open and shut case, *J. Am. Chem. Soc.* 140 (2018) 15889–15903.
- [40] Y.S. Kulkarni, T.L. Amyes, J.P. Richard, S.C.L. Kamerlin, Uncovering the role of key active-site side chains in catalysis: an extended Bronsted relationship for substrate deprotonation catalyzed by wild-type and variants of triosephosphate isomerase, *J. Am. Chem. Soc.* 141 (2019) 16139–16150.
- [41] A. Romero-Rivera, M. Corbella, A. Parracino, W.M. Patrick, S.C.L. Kamerlin, Complex loop dynamics underpin activity, specificity and evolvability in the ($\beta\alpha$)₈ barrel enzymes of histidine and tryptophan biosynthesis, *JACS Au* 4 (2022) 943–960.
- [42] R.M. Crean, M. Biler, M.W. van der Kamp, A.C. Hengge, S.C.L. Kamerlin, Loop dynamics and enzyme catalysis in protein tyrosine phosphatases, *J. Am. Chem. Soc.* 143 (2021) 3830–3845.
- [43] R. Shen, R.M. Crean, K.J. Olsen, M. Corbella, A.R. Calixto, T. Richan, et al., Insights into the importance of WPD-loop sequence in protein tyrosine phosphatases, *Chem. Sci.* 13 (2022) 13524–13540.
- [44] G. Jogl, S. Rozovsky, A.E. McDermott, L. Tong, Optimal alignment for enzymatic proton transfer: structure of the michaelis complex of triosephosphate isomerase at 1.2-Å resolution, *Proc. Natl. Acad. Sci. USA* 100 (2003) 50–55.
- [45] H.M. Berman, J. Westbrook, Z. Feng, G. Gilliland, T.N. Bhat, H. Weissig, et al., The Protein Data Bank, *Nucleic Acids Res.* 28 (2000) 235–242.
- [46] T.A.S. Brandão, A.C. Hengge, S.J. Johnson, Insights into the reaction of protein-tyrosine phosphatase 1B, *J. Biol. Chem.* 285 (2010) 15874–15883.
- [47] A.V. Due, J. Kuper, A. Geerloff, J.P. von Kries, M. Wilmanns, Bisubstrate specificity in histidine/tryptophan biosynthesis isomerase from *Mycobacterium tuberculosis* by active site metamorphosis, *Proc. Natl. Acad. Sci. U.S.A.* 108 (2011) 3554–3559.
- [48] W.L. Jorgensen, D.S. Maxwell, J. Tirado-Rives, Development and testing of the OPLS all-atom force field on conformational energetics and properties of organic liquids, *J. Am. Chem. Soc.* 118 (1996) 11225–11236.
- [49] W.L. Jorgensen, J. Chandrasekhar, J.D. Madura, R.W. Impey, M.L. Klein, Comparison of simple potential functions for simulating liquid water, *J. Chem. Phys.* 79 (1983) 926–935.
- [50] A. Warshel, G. King, Polarization constraints in molecular dynamics simulation of aqueous solutions: the surface constraint all atom solvent (SCAAS) model, *Chem. Phys. Lett.* 121 (1985) 124–129.
- [51] J. Marelius, K. Kolmodin, I. Feiberberg, J. Åqvist, Q: A molecular dynamics program for free energy calculations and empirical valence bond simulations in biomolecular systems, *J. Mol. Graph. Model.* 16 (1998) 213–225.
- [52] D. Joseph, G. Petsko, M. Karplus, Anatomy of a conformational change: hinged “lid” motion of the triosephosphate isomerase loop, *Science* 249 (1990) 1425–1428.
- [53] J.P. Richard, T.L. Amyes, B. Goryanova, X. Zhai, Enzyme architecture: on the importance of being in a protein cage, *Curr. Opin. Struct. Biol.* 21 (2014) 1–10.
- [54] M.M. Malabanan, L. Nitsch-Velasquez, T.L. Amyes, J.P. Richard, Magnitude and origin of the enhanced basicity of the catalytic glutamate of triosephosphate isomerase, *J. Am. Chem. Soc.* 135 (2013) 5978–5981.
- [55] E.N. Gurzov, W.J. Stanley, T.C. Brodnicki, H.E. Thomas, Protein tyrosine phosphatases: molecular switches in metabolism and diabetes, *Trends Endocrinol. Metab.* 26 (2015) 30–39.
- [56] B.P. Kennedy, Role of protein tyrosine phosphatase-1B in diabetes and obesity, *Biomed. Pharmacother.* 53 (1999) 466–470.
- [57] B.J. Goldstein, Protein-tyrosine phosphatases: emerging targets for therapeutic intervention in type 2 diabetes and related states of insulin resistance, *J. Clin. Endocrinol. Metab.* 87 (2002) 2474–2480.
- [58] A. Östman, C. Hellberg, F.D. Böhmer, Protein-tyrosine phosphatases and cancer, *Nat. Rev. Cancer* 6 (2006) 307–320.
- [59] D.S. Cui, J.M. Lipchick, D. Brookner, J.P. Loria, Uncovering the molecular interactions in the catalytic loop that modulate the conformational dynamics in protein tyrosine phosphatase 1B, *J. Am. Chem. Soc.* 141 (2019) 12634–12647.
- [60] T.A.S. Brandão, S.J. Johnson, A.C. Hengge, The molecular details of WPD-loop movement differ in the protein-tyrosine phosphatases YopH and PTP1B, *Arch. Biochem. Biophys.* 525 (2012) 53–59.
- [61] S.K. Whittier, A.C. Hengge, J.P. Loria, Conformational motions regulate phosphoryl transfer in related protein tyrosine phosphatases, *Science* 341 (2013) 899–903.
- [62] M.S. Choy, Y. Li, L.E.S.F. Machado, M.B.A. Kunze, C.R. Connors, X. Wei, et al., Conformational rigidity and protein dynamics at distinct timescales regulate PTP1B activity and allostery, *Mol. Cell.* 65 (2017) 644–658, e5.
- [63] G. Moise, Y. Morales, V. Beaumont, T. Caradonna, J.P. Loria, S.J. Johnson, et al., A YopH PTP1B chimera shows the importance of the WPD-loop sequence to the activity, structure and dynamics of protein tyrosine phosphatases, *Biochemistry* 57 (2018) 5315–5326.
- [64] K.R. Torgeson, M.W. Clarkson, G.S. Kumar, R. Page, W. Peti, Cooperative dynamics across distinct structural elements regulate PTP1B activity, *J. Biol. Chem.* 295 (2020) 13829–13837.
- [65] R. Shen, R.M. Crean, S.J. Johnson, S.C.L. Kamerlin, A.C. Hengge, Single residue on the WPD-loop affects the pH dependency of catalysis in protein tyrosine phosphatases, *JACS Au* 5 (2021) 646–659.
- [66] M.M. Malabanan, M.K. Go, T.L. Amyes, J.P. Richard, Wildtype and engineered monomeric triosephosphate isomerase from *Trypanosoma brucei*: partitioning of reaction intermediates in D2O and activation by phosphite dianion, *Biochemistry* 50 (2011) 5767–5779.
- [67] Y.S. Kulkarni, Q. Liao, F. Bylén, T.L. Amyes, J.P. Richard, S.C.L. Kamerlin, The role of ligand-driven conformational changes in enzyme catalysis: modeling the catalytic case of triosephosphate isomerase, *J. Am. Chem. Soc.* 140 (2018) 3854–3857.
- [68] J. Stare, Complete sampling of an enzyme reaction pathway: a lesson from gas phase simulations, *RSC Adv.* 7 (2017) 8740–8754.